Bipolar Thermoelectrics

Sponsors
MIT Lincoln Laboratory, DARPA University Optocenters Program

Project Staff
Kevin Pipe, Professor Rajeev J. Ram, Professor Ali Shakouri (UCSC)

Thermal management is important for many microelectronic devices due to the performance losses that accompany heat generation, and is often accomplished through the use of an external thermoelectric cooler. Such coolers operate on the principle of the Peltier effect: when carriers move across a junction between two materials in which they transport a different amount of energy, heat is exchanged with the surrounding lattice to make up the difference. An alternative solution is to optimize the thermoelectric behavior of the device itself so that cooling is achieved internally.

For the fundamental case of the *p-n* diode, diffusing minority carriers must pull a large amount of heat energy out of the lattice near the junction in order to move against the built-in field. Under optimal conditions for the diode's dimensions and doping, this bias-dependent heat exchange term can be large enough to cause a significant drop in the junction temperature [1]. As shown in Figure 1, a range of current bias exists for which thermoelectric cooling dominates Joule heating. Figure 2 demonstrates the large temperature differences that can be achieved in materials that have high mobility and low thermal conductivity. Such cooling can be enhanced using heterojunctions and can be an important design consideration for devices such as diode lasers.

References

1. K. P. Pipe, R. J. Ram, and A. Shakouri, "Bias-dependent Peltier coefficient and internal cooling in bipolar devices", *Phys. Rev. B* **66**, 125316 (2002).

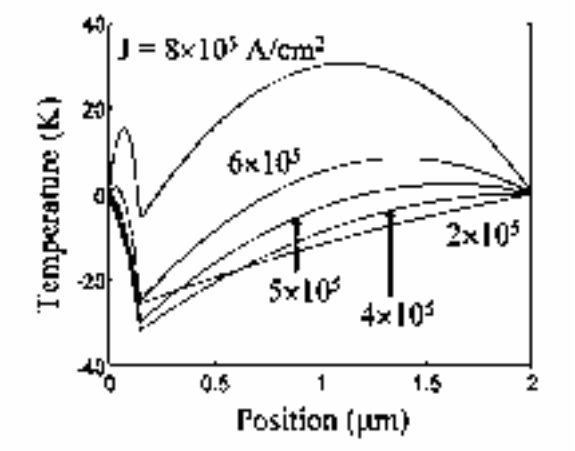

Fig. 1: Internal temperature profile (with respect to $T_0 = 0$) at several values of current bias for a 2μm $Hg_{0.8}Cd_{0.2}Te$ diode doped symmetrically at 1×10^{19} cm^{-3}, assuming optimal diode width. The internal temperature minimum occurs at the junction.

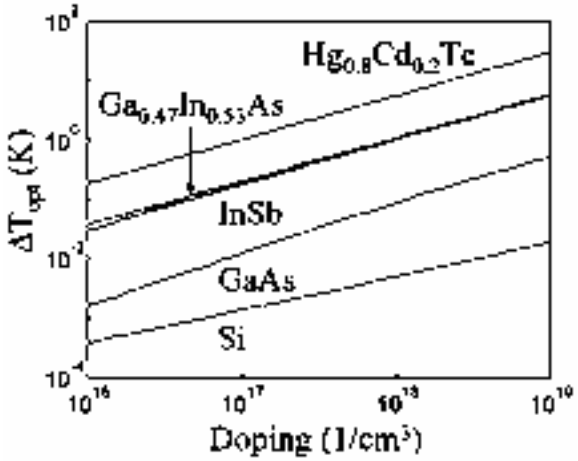

Fig. 2: Optimal internal temperature drop for several semiconductor diode materials.

Thermal Probing of Semiconductor Devices

Research Staff
Professor Janice A. Hudgings, Professor Rajeev Ram

Sponsors
DARPA: University Optocenters Program

Temperature profiling is of substantial interest in improving thermal design of optoelectronic devices such as electroabsorption modulators and diode lasers [1-3]. We demonstrate the utility of thermal profiling as a non-invasive technique for wafer-scale testing of the optical power distribution in photonic integrated circuits. By spatially profiling the heat exchange of a system of cascaded optical devices with its environment, the optical distribution in the individual components, as well as a wide variety of intrinsic device parameters, can be precisely quantified over a wide range of operating conditions.

We demonstrate this thermal profiling technique using optical injection into the waveguide of a laser diode. The 50x600 μm^2 5-QW InGaAsP/InP, cleaved-facet laser with gain peak at 1.54 μm is mounted on an actively temperature controlled copper block. A microlensed fiber is used to inject light from an external source into one end facet of the waveguide. 25x25 μm^2 NIST-traceable thermocouples with an accuracy of 10 mK are used to monitor the surface temperature of the device as a function of distance from the input facet, the heat sink temperature, and the ambient temperature; typical results are shown in Figure 3.

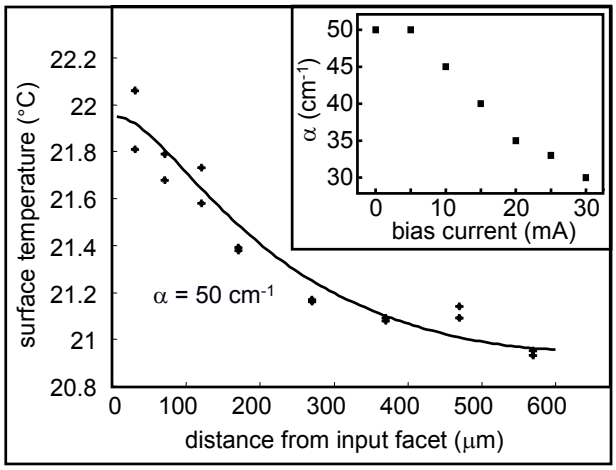

Fig. 3: Measured (dots) and modeled (solid line) temperature profile of an optically injected diode laser biased below threshold to act as an absorber. Inset shows the measured dependence of absorption on the bias current.

We use a finite element heat balance model to describe the thermal profile of the device [2]. The model can be used to extract the absorption coefficient of the waveguide if the remaining physical parameters are known. The vertical thermal impedance Z_T=33 K/W and the product $A_{eff}h=4.5x10^{-3}$ W/K, where A_{eff} is the planar surface area and h is the heat transfer coefficient, can be found using the techniques of Reference 2. We determine the lateral thermal impedance using a hot spot measurement in which a hot probe tip is used to heat a roughly 20x20 μm^2 area at one end of the laser, which is operated below threshold and without optical injection. By measuring the surface temperature as a function of the distance from the hot spot, we extract Z_{Tlat} = 5000 ± 1000 K/W from our model. This value is in excellent agreement with the lateral impedance predicted by comparing a finite element solution to the standard heat equation $\nabla \bullet k\nabla T = -q$, accounting for the various material layers of the device, to the experimental data.

Using these material parameters, the absorption coefficient α of the waveguide can be extracted by fitting the model to the experimental data; see Figure 3. We estimate the uncertainty of α using this technique to be ±10%, limited mainly by the size of the thermocouples. The inset of Figure 3 shows the measured absorption of the laser over a range of bias currents; this data agrees well with independent measurements using the Hakki-Paoli method [4].

In conclusion, spatially resolved thermal profiling is a powerful technique for wafer-scale, non-invasive mapping of the optical power distribution inside photonic integrated circuits. Using thermal imaging or thermal reflectance techniques to record the thermal profile would enable rapid characterization of complex photonic circuits [3].

References

1. T. Ouchi, "Thermal analysis of thin-film vertical-cavity surface-emitting lasers using finite-element method," *Japanese Journal of Applied Physics*, vol. 41, pp. 5181-5186, 2002.

2. K.P. Pipe and R.J. Ram, "Experimental determination of heat flow in semiconductor lasers," presented at Conference on Lasers and Electro-Optics, Long Beach, CA 2002.

3. A. Shakouri, J. Christofferson, and Z. Bian, "High spatial resolution thermal imaging of multiple section semiconductor lasers," presented at Photonic Devices and Systems Packaging Symposium, Stanford, CA 2002.

4. E.K. Lau, "Analysis of 1.55 μm semiconductor lasers for modelocked operation," Ph.D. thesis in Electrical Engineering and Computer Science, Cambridge: Massachusetts Institute of Technology, 2001, pp.194.

Electro-Thermal Modeling of Semiconductor Lasers

Sponsors
MIT Lincoln Laboratory, DARPA University Optocenters Program

Project Staff
Kevin Pipe, Professor Rajeev J. Ram

Heat management can be a critical issue in semiconductor diode laser design due to the strong temperature dependencies of threshold current, quantum efficiency, and device lifetime. Mid-infrared antimonide-based sources are particularly susceptible to thermal rollover due to weak carrier confinement and large nonradiative losses through processes such as Auger recombination.

In order to study the electrical and thermal properties of semiconductor lasers, we examine two strained single-quantum-well lasers, one an oxide-stripe device and the other a ridge-waveguide device, which are both grown on GaSb substrates. To model the devices' electrical properties, we solve the drift-diffusion equations self-consistently with Poisson's equation. As shown in Figure 4, experimental measurements of the I-V relations for the devices are consistent with the model. After modeling carrier flow (and therefore heat source distribution) in the devices, we proceed to a finite-element thermal model to solve for the temperature distribution. We verify this thermal model by using microthermocouple probes to measure the lasers' surface temperature; the results are shown in Figure 5. Having developed models that rely only on published material parameters and do not rely on fitting parameters, we can extract properties such as the thermal impedance and can examine the relative magnitudes of the heating processes in the devices with some degree of confidence [1]. We can furthermore apply these models in the design process to improve the lasers' thermal performance [2].

References

1. K. P. Pipe, R. J. Ram, A. K. Goyal, and G. W. Turner, "Electrical and thermalanalysis of heat flow in λ=2.05μm GaInAsSb/AlGaAsSb lasers", Conf. onLasers and Electro-Optics, Baltimore, MD, June 2003.

2. K. P. Pipe, R. J. Ram, and A. Shakouri, "Internal cooling in a semiconductorlaser diode", *IEEE Phot. Tech. Lett.* **14**, 453 (2002).

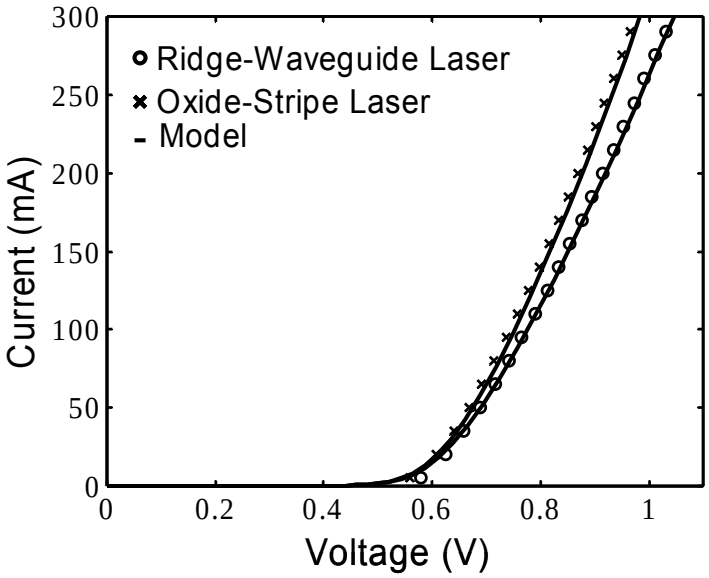

Fig. 4: Current and voltage characteristics of ridge-waveguide and oxide-stripe lasers, both modeled and measured experimentally.

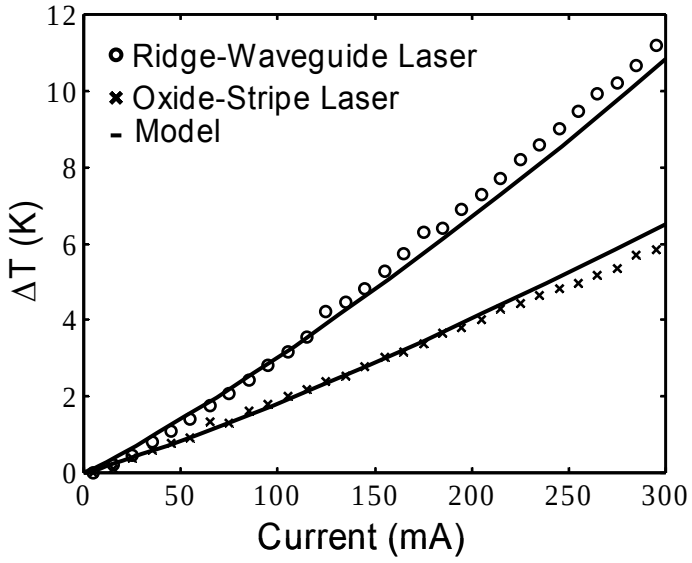

Fig. 5: Modeled and measured top-side to bottom-side temperature difference.

Waveguide Optical Isolators

Sponsor
Walsin Lihwa

Project staff
Dr. Xiaoyun Guo, Tauhid Zaman, Professor Rajeev Ram

An optical isolator is a device that transmits light in only one direction. Optical isolators are required in optical communication systems to protect laser sources and optical gain elements. Available microoptic isolators are bulky and require expensive alignment. A waveguide isolator which can be integrated with the source and other waveguide devices will be necessary for integrated photonics circuit.

A nonreciprocal polarization rotation is the key to an isolator's performance, i.e. coupling between TE and TM mode. Faraday rotation is a well known nonreciprocal polarization rotation. The coupling ratio *R* is calculation as

$$R = \frac{F^2}{F^2 + (\Delta\beta / 2)^2},$$

where *F* is the Faraday constant and $\Delta\beta = \beta_{TE} - \beta_{TM}$ is the difference in the TE and TM propagation constants. We have observed Faraday rotation in doped InP with a Verdet coefficient of ~ 2.4°/mm/T (Fig. 6) and a loss of 0.2cm^{-1} at 1550nm. The Verdet coefficient is the Faraday constant divided by the magnetic field intensity. In a waveguide with birefringence, the incomplete conversion of TE to TM and vice versa will confine the polarization rotation within a small angle. Thus a waveguide is required to have the same propagation constants for both TE and TM modes.

Birefringence arises from different sources including stress and waveguide geometry. We have developed techniques to fabricate birefringence free ridge waveguides. The waveguides consist of an InGaAsP core layer and InP cladding layers. Stress and photoelastic birefringence are negligibly small. To eliminate the shape birefringence, the ridge waveguide is designed to have a certain width and etching depth. In our process, high index contrast mesa is used. A 100nm Ti film is used as an etching mask. The ridge waveguide is etched using reactive ion etching with a mixture of hydrogen and methane. Fig. 7 is an SEM micrograph of the ridge waveguide and Fig. 8 shows the calculated geometric parameters for a birefringence free waveguide. The numerical simulation was performed using code developed by Mike Watts and Hermann Haus at MIT.

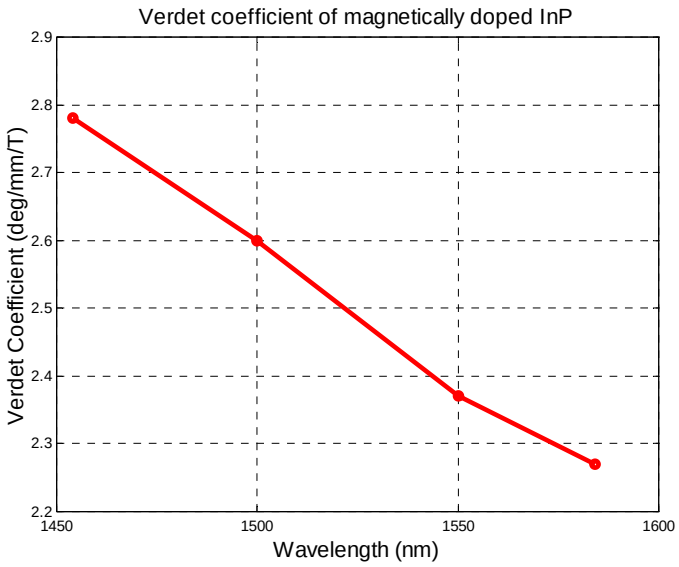

Fig. 6: Verdet coefficient of magnetically doped InP

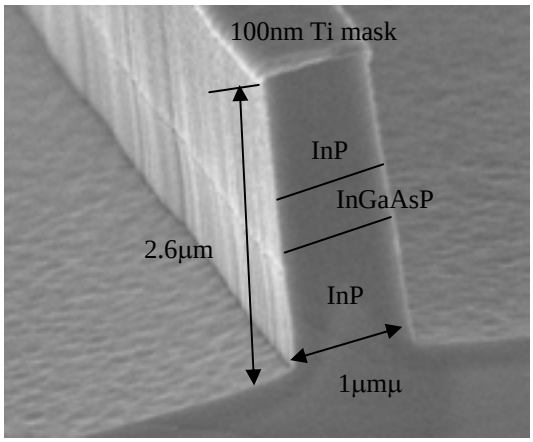

Fig. 7: SEM micrograph of a RIE etched ridge waveguide

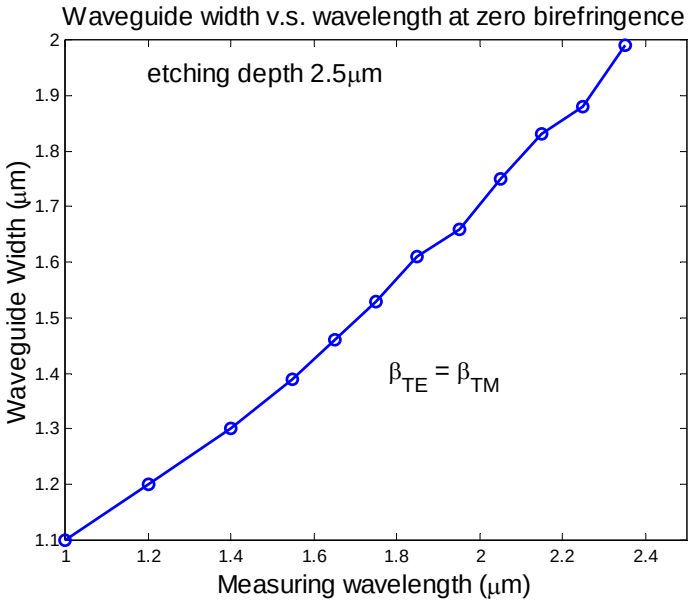

Fig. 8: Zero birefringence calculation for different waveguide widths and measuring wavelengths (2.5 μm etching depth for all waveguides)

Pulsed-light absorption induced disordering for quantum well intermixing

Sponsor
DARPA and Walsin Lihwa Corp.

Project Staff
Song-Ho Cho, Professor Rajeev J. Ram

Collaborators
Ryan Thom, Dr. Jurgen Michel

As photonic integration becomes increasingly important in years to come, its development will focus primarily on planar lightwave integrated circuits on InP for integrating active and passive devices in a single wafer. Monolithic integration of several photonic devices, so called photonic integrated circuits (PIC), contain optically interconnected devices that reroute, condition, or process the signal while still in its optical form of photons. PICs offer the promise of superior performance, compact size, reliability, cost reduction, low power consumption, and increased packaging robustness without the complicated network fiber links. However, there are engineering challenges in PICs that should be overcome to combine active photonic sources, passive waveguides, at micron dimensions. Furthermore, bandgap engineering is critical to realizing the potential benefits of PIC, because the different active and passive devices need different band gaps within the epiwafer. Conventionally, the process for fabricating PICs with different bandgaps consists of three steps: patterning, etching out the unwanted epitaxial layers, and subsequent selective epitaxial regrowth over the entire wafer, which is complex and cumbersome and requires a fair amount of finesse.

A promising approach to introducing different bandgaps on one wafer is quantum well intermixing (QWI) that emerges as a powerful technique for fabricating PICs as well as generates considerable interest due to its simplicity.[i] QWI is a post-growth technique that allows the bandgap energy of an existing quantum well to be selectively modified using only one epitaxial step without use of epitaxial-regrowth process. QWI slightly changes the composition of the interface between the quantum well and barrier layers through a process of controlled lattice disordering to form a new alloy. Essentially, QWI utilizes point defects such as vacancies or interstitials of interdiffusing lattice atoms. The intermixing mechanism between the quantum well (QW) and barrier is based on the fact that a QW is an inherently metastable system due to the large concentration gradient of atomic species across the QW and barrier interface in a distance of less than 1 nm. At high temperatures, significant diffusion of atomic species hopping from one lattice to another lattice site will occur resulting in an intermixing of the QW and adjacent barrier materials. This process provides a route to fabricating low-loss optical waveguides, modulators, lasers and, detectors, using only one epitaxial step. The key advantage of this technology is that different bandgap sections or different wavelength interfaces are aligned perfectly each other. Since the adiabatic transition in refractive index step can be achieved in a butt joint between active and passive regions, the reflection coefficient can be reduced to 10^{-5}. Recently, three different QWI methods by which the defects are introduced have been developed, including impurity-induced disorder, impurity free vacancy disorder either by dielectric cap or ion implantation, and laser or photoabsorption induced disorder.

The main advantage of photo-absorption induced disordering (PAID) technique is its selective interdiffusion of different QW layers. The absorption of high-energy photons from a laser causes bond breaking and lattice disruption in the sample, which lead to an increase in the point defect density. The poor thermal stability of the InGaAs-InGaAsP system has been used to great advantage in the PAID process, in which photons from a 1064 nm Nd:YAG laser are preferentially absorbed within the InGaAs-InGaAsP QW region. To achieve high spatial separation between intermixed and as-grown regions, Q-switched laser pulses are used, because continuous irradiation of laser beams thermally anneals in large lateral dimension. A Q-switched Nd:YAG laser in MIT's Harrison Spectroscopy Lab with a pulse width of few nanoseconds is used.

Subsequent high temperature annealing results in diffusion of the point defects and enhances the QWI rate. During annealing, the sample was sandwiched between two pieces of fresh InP substrates to provide P overpressure, so that the diffusion of P from the surface would be minimized during annealing.

Fig. 9 shows the measurement of blue-shifted catholuminescence spectra, depending on the different annealing durations with the exposure condition of fluence, 2 mJ/mm$_2$ by Q-sw Nd:YAG laser beam onto the multi QW sample. The maximal peak shifts of 50 nm were observed, while the full-width half-maximum of all spectra were maintained less than 50 nm throughout different thermal annealing conditions, which demonstrates high quality QWI in InGaAsP quantum wells and InGaAsP barriers.

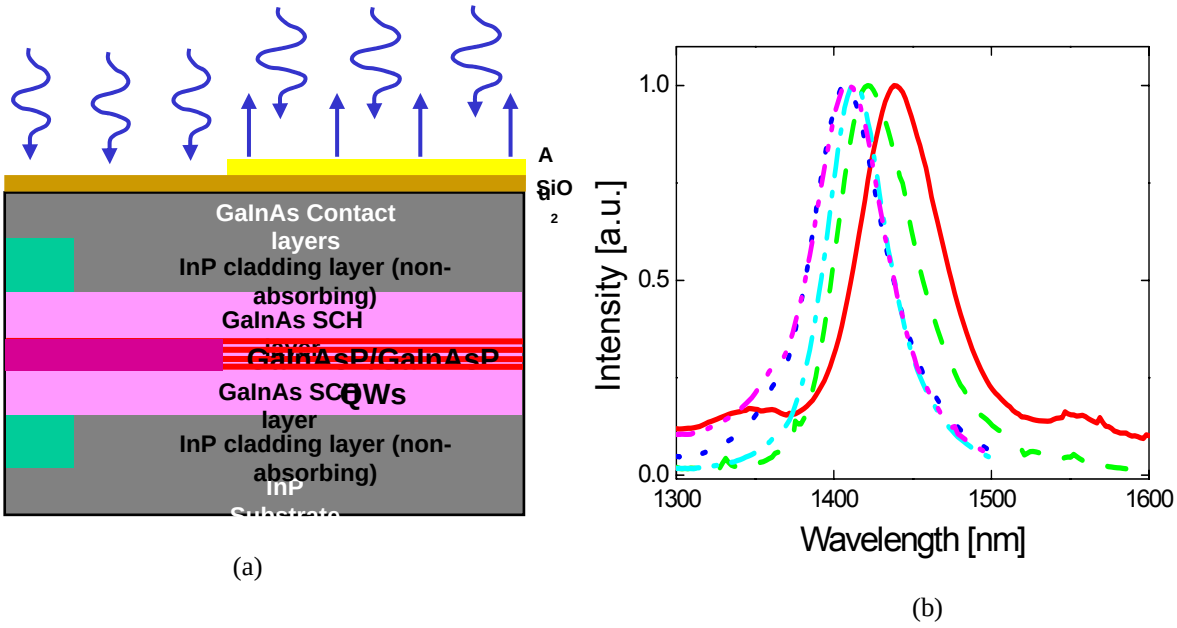

(a) (b)

Fig. 9: (a) Layer structure of the sample: most of the point defects are only created in the absorptive quantum well layers where pulsed light beams transmit through SiO_2 antireflection coating. (b) Catholuminescence spectra measured at 20 K, after 650ºC rapid thermal annealing, showing a maximal peak shift of 50 nm. A group of spectra indicates different rapid thermal annealing durations; 1 min (solid line); 2 min (dash line); 3 min (dot line); 6 min(dash-dot line); 10 min (dash-dot-dot line).

Power Dissipation in Optical Network Components

Research Staff
Katherine Butler, Professor Rajeev J. Ram

Sponsor
Microphotonics Center Industry Consortium

Power consumption is a growing concern in the telecommunications industry. Data centers consumed an average of 10 to 40 megawatts of power in the US as reported in 2002 [1]. This research project attempts to address the issue of power consumption and overall energy efficiency by analyzing the power consumption in optical networks from a component perspective. The project focuses on analyzing power dissipation and energy efficiency in transponder/transceiver modules. Figure 10 shows a comparison of two transceiver modules, one at 2.5 Gb/s and the other at 10 Gb/s.

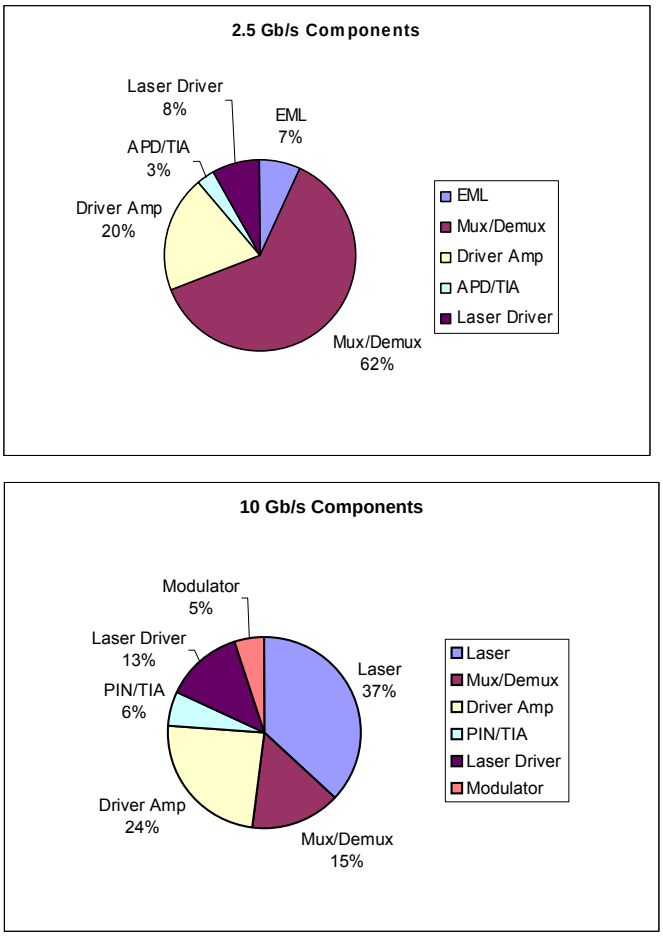

Fig. 10: Power Comparison of 2.5 Gb/s and 10 Gb/s Transceivers [2,3]

This comparison identifies the electrical multiplexer/demultiplexer, the driver amplifier, and the thermoelectric cooler in the laser, as the components that are responsible for most of the power consumption within the transceiver. Scaling relationships for the power dissipation with the bit rate and with improvements in component design are developed. For example, a 2.5 Gbps 16:1 transponder using an uncooled electro-absorption modulated laser as the transmitter has a typical overall power consumption of 4-5 W, compared to 10 W for the 10Gbs module. The dramatic reduction in power dissipation originates from the ability to use an uncooled source at 2.5 Gbps and also a reduction in the drive voltage for the electro-absorption modulator relative to the lithium niobate modulator at 10 Gbps. Removing the TE cooler saves approximately 3 W and the lower speed, lower voltage driver amplifier requires 2-3 W less power. This analysis has recently been extended to a study of the limitations on optoelectronic integration set by the disspiated power density. This analysis is being extended to a study of the limitations on optoelectronic integration set by the disspiated power density.

References

[1] Miller, Rich. “Utilities: Skepticism Pays Off” March 2002
http://www.carrierhotels.net/news/March2002/imnutilities.shtml

[2] For example JDSU 54TR

[3] For example Intel TXN13500

Communications Technology Roadmap

Research Staff
Elizabeth Bruce, Professor Rajeev J. Ram

Sponsor
Microphotonics Center Industry Consortium

The goal of the MIT Microphotonics Communications Technology Roadmap is to develop a roadmap for the integration of opto-electronic components for communications. The project is unique in that it incorporates a deep understanding of the underlying photonic technologies with a comprehensive view of the entire communications value chain, including industry, business, and policy dynamics. Roadmapping can serve as a powerful tool for academia, business and government by helping focus technology development efforts, guide allocation of resources, and direct financial investment.

During the summer of 2002, we established a series of Technology Working Groups (TWG) to focus on specific platforms for integrated opto-electronic circuits. These working groups include both academic and industry participants. We currently have four on-going TWGs focused on the following platforms: Silicon, III-V materials, Organics, and Hybrid Integration. Figure 11 shows the basic opto-electronic functions incorporated in a DWDM optical networking transponder – these functions will be used as the key building blocks for integration.

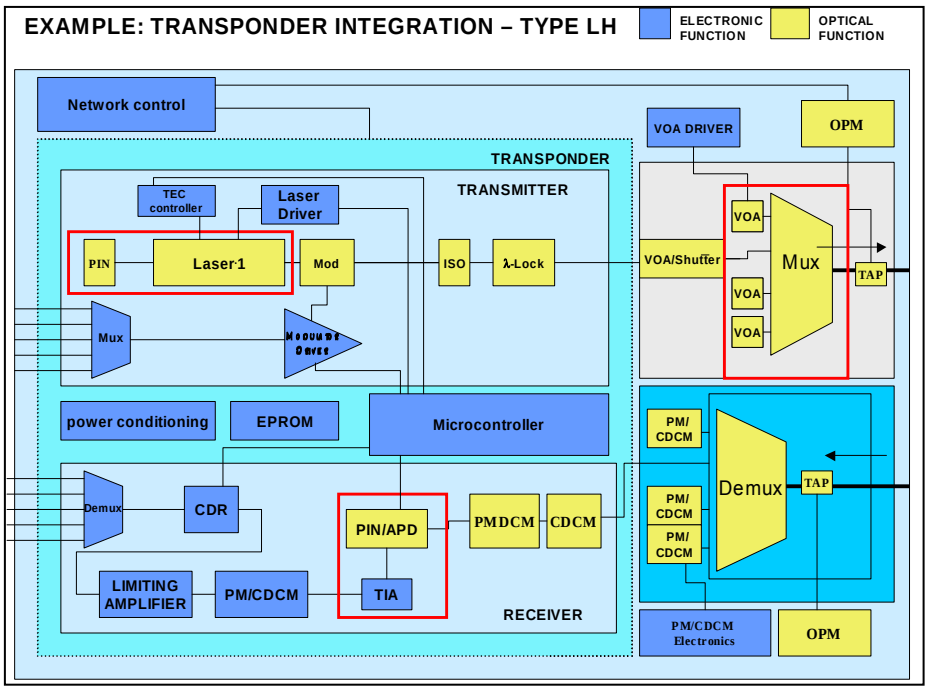

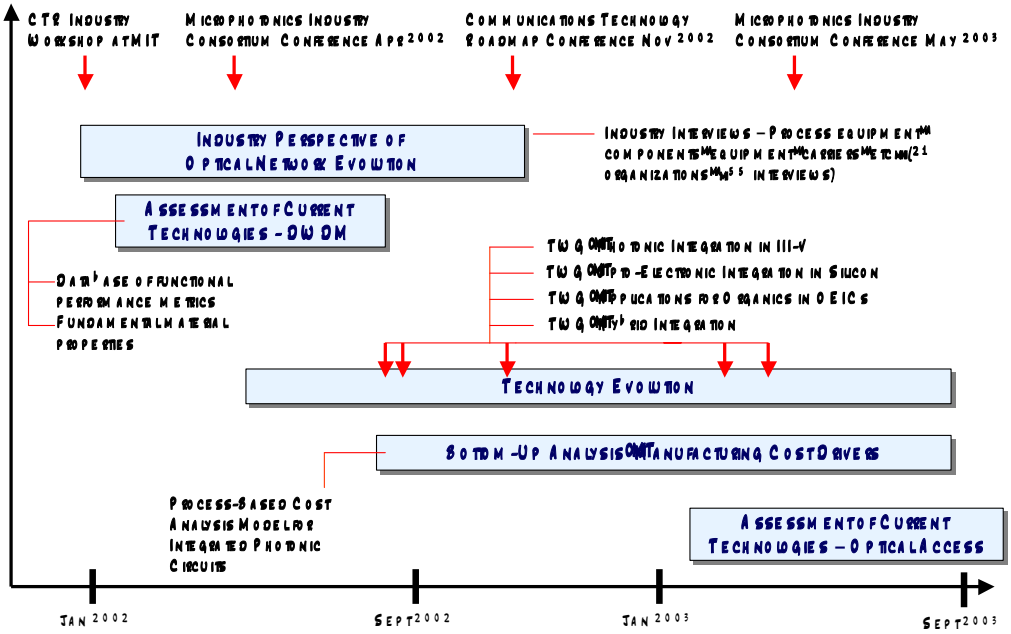

In addition to the Working Groups, the Communications Technology Roadmap project has various on-going research projects involving both Engineering and Sloan school students. Figure 12 highlights some of the major on-going projects over the last year. More information on the project is available at http://mph-roadmap.mit.edu.

Hot Electron Transport in Two-Dimensional Electron Gas Wires

Research Staff
Mathew C. Abraham (Harvard), Professor Rajeev.J. Ram, James Daley, Professor Henry I. Smith, Dr. K. Maranowski (UCSB), Professor A. C. Gossard (UCSB).

Sponsor
National Science Foundation

Hot electron transport in two-dimensional electron gases (2DEGs) has been studied extensively [1][2] and diverse explanations have been provided for the I-V curves that have been measured for various samples. The experiment and analysis presented here deal with 2DEG wires defined using electrostatic gates in AlGaAs/GaAs modulation doped heterostructures. A micrograph of the 4μm wide and 150μm long wire is shown in Figure 13. The 2DEG sample was measured to have a bulk electron concentration $n=2.0\times10^{15}/m^2$ and mobility $\mu=80m^2/Vs$ at 10K.

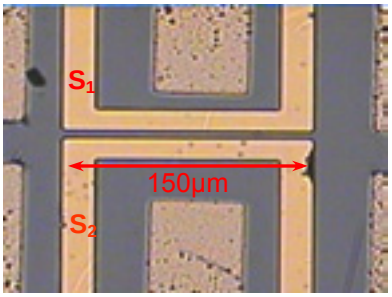

Fig. 13: Gold gates S_1 and S_2 electrostatically define a 4μm wide, 150μm long, 2DEG wire in a modulation doped AlGaAs/GaAs heterostructure.

As expected for high mobility 2DEG wires, the data shown in Figure 14 displays the approximately linear dependence of dV/dI on lattice temperature for various bias currents, as acoustic phonon (e-p) scattering is the dominant scattering mechanism in this temperature range [2][3]. It is interesting to note that even for high bias currents (hot carriers), the linear dependency to T_L is maintained.

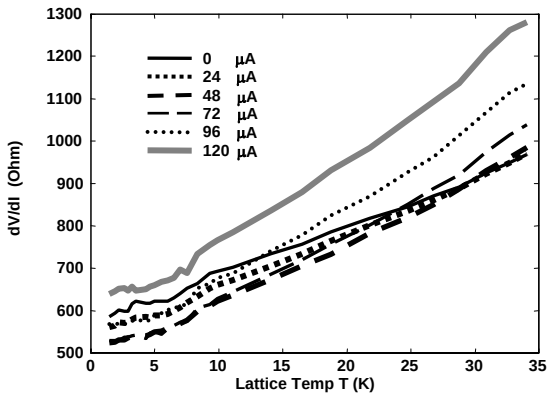

Fig. 14: The data shows the approximate linear dependence of the resistance of the wire as a function of lattice temperature even for large bias currents.

Typical differential resistance dV/dI vs. I curves for various lattice temperatures T_L are shown in Fig. 15. The striking feature in the data is that for T_L < 34K, there is a distinct peak in the resistance centered around zero bias. This fall in resistance with increasing current can be attributed to the reduction in electron-impurity (e-i) scattering as the electron temperature, T_e, rises [3]. For large current biases, phonon emission becomes an important momentum relaxing process and therefore the resistance eventually rises for currents greater than 60μA even though (e-i) scattering continues to diminish.

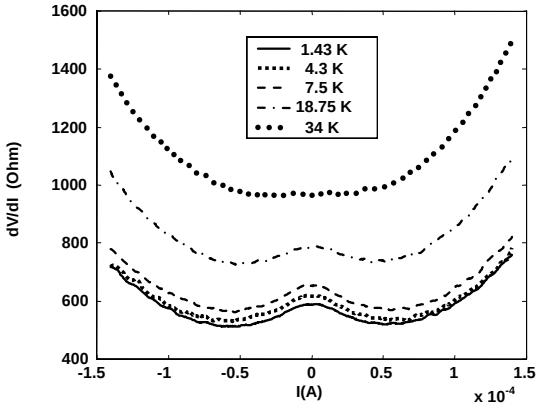

Fig. 15: Resistance of the wire as a function of bias current shows a beak centered around zero current for lattice temperatures below 34K.

The device studied here is similar to Ref. [4], the only difference being the higher mobility (in Ref.[4] the bulk mobility was between 170 and 210 m^2/Vs). De Jong et al. [4] explain a similar reduction in resistance in their data by arguing that a subtle hydrodynamic effect which involves the interplay between electron-electron (e-e) scattering and electron-boundary (e-b) scattering causes a reduction in resistance as a function of bias current. However, the hydrodynamic effect as described in Ref. [4] is not the dominant effect since the electrons colliding with the electrostatically defined gates suffer mainly specular reflections [5] that conserve momentum in the direction of the current and therefore produce only minimal drag. Also, the e-e scattering length of the device used in Ref. [5] is not small enough to create an effective viscosity to enable fluid like behavior. Additionally, our analysis of the electron temperature dependence of the impurity scattering supports the interpretation that the change in the relative strengths of electron-phonon and electron-impurity scattering contributes to the rising mobility.

In addition to developing a quantitative theoretical model to explain our data, we are also investigating, for low lattice temperatures (<4K) and for small bias currents (<10 μA), the existence of a rising resistance that can be associated with the Bloch-Grüneisen regime [2].

References

[1] Jagdeep Shah, *IEEE J. Quantum Electron., **QE-22** (9) p1728 (1986), and references there in*.
[2] Peter J. Price, *J. App. Phys., **53**(10) p 6863 (1982), and references there in.*
[3] W. Walukiewicz, H. E. Ruda, J. Lagowski, and H. C. Gatos, *Phys. Rev. B, **30**(8) p4571.*
[4] M.J.M. de Jong and L. W. Molenkamp, *Phys. Rev. B, **51**(19) p13389 (1995).*
[5] T.J.Thornton, M.L. Roukes, A.Scherer, and B. P.Van de Gaag, *Phys. Rev.Lett., **63** (19) p2182 (1989).*

Manipulation of Nanoparticles

Research Staff
Brian Goldberg, Professor Rajeev J. Ram

Sponsor
Packard Foundation, National Science Foundation Center for Materials Science and Engineering

We report on the manipulation of 5nm cobalt nanoparticles using an Atomic Force Microscope (AFM). The particles are synthesized in Professor Moungi Bawendi's group in the department of chemistry at MIT. The particles consist of a cobalt core surrounded by a thin layer of organic surfactant that prevents oxidation and agglomeration of the particles in solution. The particles are spin coated onto a mica substrate before imaging and manipulation.

The particles are imaged with a Digital Instruments Dimension 3100 AFM with the new Nanomanipulation (NanoMan) extension module. NanoMan provides closed loop feedback control for sub-nanometer positioning of the AFM tip. After initial imaging the AFM tip is lowered onto the substrate and literally pushes against the particle. The bulldozer-like nature allows for manipulation of particles on the nanometer scale.

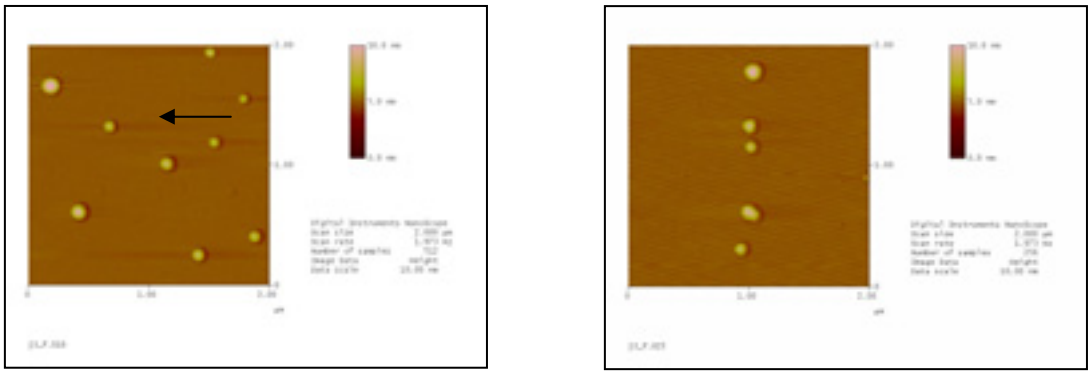

Fig. 16: (A) Initial AFM image showing 9 nanoparticles in a 2 x 2 μm^2 region. The arrow indicates the direction of the AFM tip during the first move. (B) After image. The particles were moved into a straight line.

Optical Sensing of Bioprocesses

Research Staff
Harry Lee, Professor Rajeev J. Ram, Nathalie Gorret, Professor Anthony J. Sinskey

Sponsor
DuPont MIT Alliance

An ideal bioprocess monitoring tool would be able to analyze all components in bioprocess media with high sensitivity *in-situ*, which would eliminate errors due to physiological disturbance during sampling, reduce contamination risk, and allow higher measurement frequency. As a non-invasive optical technique, Raman spectroscopy has the potential for approaching this ideal tool. However, to realize this potential will require developing a method to achieve reliable concentration estimations from Raman spectra collected through scattering media with widely varying optical density, and quantifying sensitivity limits and sources of error. To resolve these issues, we are focusing on explicit least squares methods, which do not require a lengthy calibration process and can tolerate the widely varying optical densities encountered during fermentations.

In preliminary experiments on samples taken from an isoleucine producing *Corynebacterium* fermentation on defined medium, we have used an explicit least squares method, including the pure spectra of all significant bioprocess and background components, and basis functions for a fourth order polynomial to account for background fluorescence. Scattering correction is implemented by accounting for attenuation by internal reference to the least squares estimated water component, and wavelength dependent scattering can be corrected by adjusting the basis spectra. Fig. 17 a,b) shows measured Raman spectra from filtered samples of fermentation medium at the beginning of the fermentation and after 18 hours of growth. Raw data, the least squares reconstruction, the least squares reconstruction with background components removed, and the residual, or difference between the model fit and the measured data. Part c) shows the pure components included in the least squares modeling.

Fig.18 shows glucose and isoleucine concentrations from reference HPLC measurements and Raman estimated concentrations for samples without cells, with cells, and with cells including scattering attenuation correction. The inset shows the 1cm optical density of the samples. While the

concentration estimates in the scattering attenuation corrected data have an absolute additive error, the rate of substrate consumption and product formation is properly estimated.

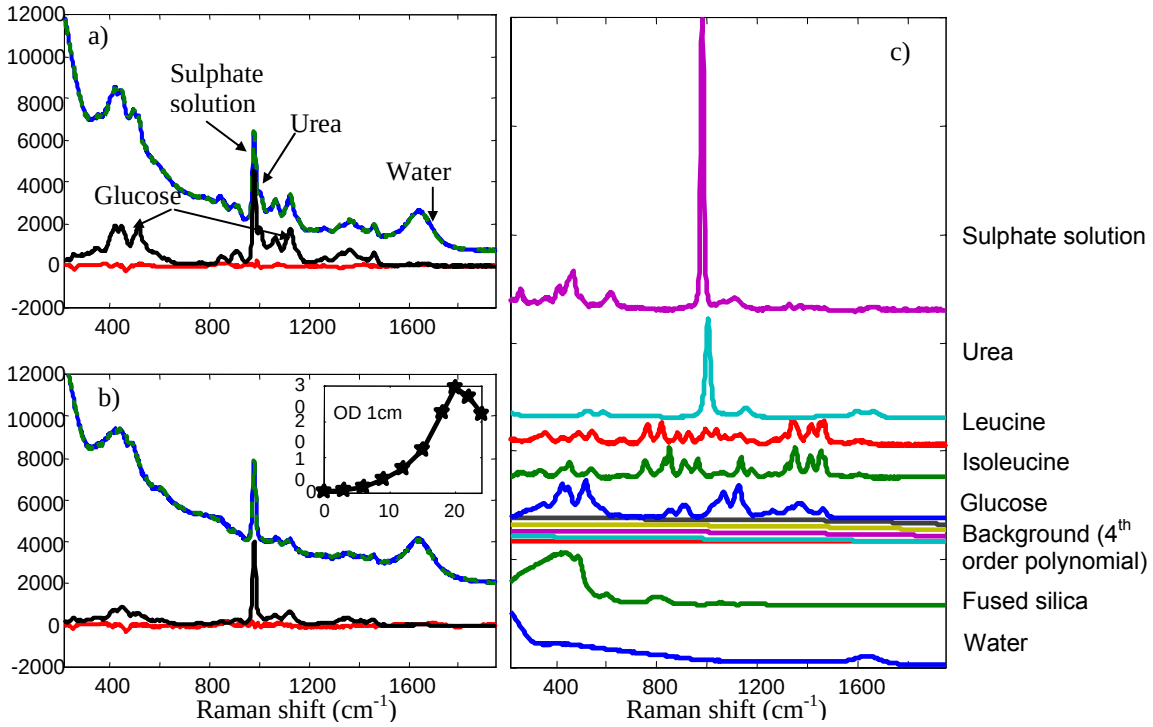

Fig. 17: a,b) Raman spectra from filtered fermentation medium initially (a) and after 18 hours of cell growth (b). The upper solid line is measured data, the upper dashed line is the least squares model reconstruction, the lower solid line is the reconstruction excluding background components and the bottom solid line is the residual, or difference between model fit and measured data. The inset of b) shows the growth curve of the bacteria culture. Part c) shows the pure spectra and background components included in the model.

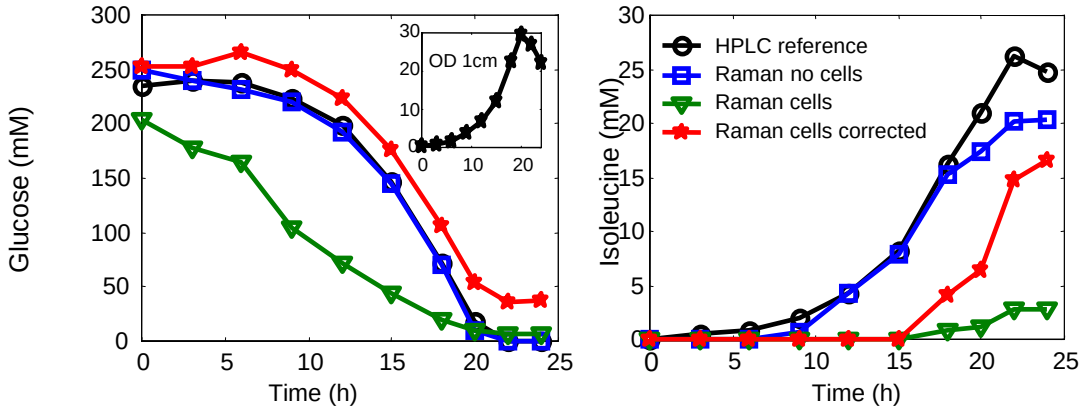

Fig. 18: Glucose and isoleucine concentrations from reference HPLC measurements (circles) and Raman estimated concentrations for samples without cells (squares), with cells (triangles), and with cells including scattering attenuation correction (stars). The inset shows the 1cm optical density of the samples.

[i] A. McKee, C. J. McLean, G. Lullo, A. C. Bryce, R. M. De La Rue, J. H. Marsh, and C. Button, "Monolithic Integration in InGaAs/InGaAsP Multiple-Quantum-Well Structures Using Laser Intermixing," *IEEE Quantum. Electron.* **33**, 45 (1997).